Correspondence to:
H. L. Roman-Stork,
hromanstork@seoe.sc.edu

Analysis of Coupled Oceanic and Atmospheric Preconditioning for Primary Madden-Julian Oscillation Events Across ENSO Phases

Casey G. Shoup[1] [iD], Heather L. Roman-Stork[1] [iD], and Bulusu Subrahmanyam[1] [iD]

[1]School of the Earth, Ocean, and Environment, University of South Carolina, Columbia, SC, USA

Abstract The Madden-Julian Oscillation (MJO) is the dominant mode of air-sea interaction over intraseasonal timescales. The effects of the MJO are well understood, but the initiation of the MJO remains less conclusive, particularly under El Niño Southern Oscillation (ENSO) conditions. Primary MJO events are those not immediately preceded by existing MJO activity of sufficient strength. As they are rare by definition, primary MJOs remain difficult to study, especially so when observations of events are scarce and of low spatiotemporal resolution. The advent of satellites allows for more expansive observations to be made more frequently than in situ methods, thus improving the observational capabilities of pre-primary MJO conditions in the ocean and atmosphere. We examined oceanic and atmospheric intraseasonal signals preceding two primary MJO events during contrasting ENSO events in an attempt to bridge the connection between oceanic and atmospheric observations as potentially coupled trigger mechanisms. Satellite observations and model simulations of the central and western Indian Ocean show that intraseasonal peaks in absolute dynamic topography (ADT) and sea surface temperature (SST) upward of 1 to 2 weeks prior to the observed outgoing longwave radiation (OLR) minimum. Surface ocean warming moistens the near surface through anomalous surface fluxes, which destabilizes the lower atmosphere to deep convection. Low-level moisture flux convergence (MFC) moistens the lower atmosphere prior to convective initiation, thus forcing an increase of total column moist static energy (MSE). Coupled midtropospheric cooling is observed that further destabilizes the atmosphere. Zonal shifts in contributing initiating parameters are observed during ENSO phases.

Plain Language Summary As an eastward propagating band of alternating strong and weak convective activity, the Madden-Julian Oscillation (MJO) dominates tropical Indian Ocean intraseasonal variability. The initiation of the MJO is heavily debated, although evidence suggests that the ocean and the atmosphere both play a significant role in contributing to the initiation of MJO events. By examining the ocean and atmosphere simultaneously using satellite observations and model output, we can determine relative preconditioning in the ocean and atmosphere and how those signals contribute to MJO convective growth. Although the atmospheric signals in moisture availability are more robust, intraseasonal variability in ocean heat content and sea surface temperature create the conditions necessary for primary MJO initiation in the atmosphere. Air-sea coupling relative to the initiation of primary MJO events over the tropical Indian Ocean is evident in both satellite observations and model output with observed variability across El Niño and La Niña phases. It is critical that we understand how primary MJO events and ENSO phases interact in order to improve the forecasting and monitoring of these events in the Indian Ocean.

1. Introduction

The tropical oceans experience strong variability patterns, especially over intraseasonal timescales. The most dominant form of tropical intraseasonal variability is that of the Madden-Julian Oscillation (MJO; Madden & Julian, 1971, 1972, 1994). The MJO is characterized and observed as an eastward propagating band of high and low convective activity that typically propagates at 3–5 m s^{-1} across the equatorial Indian and Pacific Oceans, although its effects can be observed on global scales (Zhang, 2005). The MJO is considered to be a primarily atmospheric phenomenon but can be monitored and detected in oceanic and atmospheric parameters simultaneously as a coupled air-sea event. Model simulations have expressed the importance of near surface fluxes in modulating MJO convection and propagation, suggesting that accurate MJO prediction requires that the ocean be considered in forecasts (Inness & Slingo, 2003; Inness et al., 2003), especially

when sea surface temperature (SST) is high and able to actively contribute to MJO convective initiation by increasing moisture availability (Arnold et al., 2013).

As such, it is increasingly important to monitor the ocean and atmosphere such that neither is discounted. Where observations were once scarce and of low resolution, satellites have improved the observational capabilities of the MJO. Improved parameterization techniques throughout the years have been able to enhance the observed intraseasonal MJO response, especially in sea surface salinity (SSS; Grunseich et al., 2013; Shoup et al., 2019). Satellites have also paved the way to study intraseasonal oscillations in new ways, such as through satellite-derived altimetry (Grunseich & Subrahmanyam, 2012; Trott & Subrahmanyam, 2019). In addition, the zonal structure and propagation of the MJO have been studied using satellite-derived rainfall from the Tropical Rainfall Measuring Mission (TRMM; Morita et al., 2006), which further indicates the capabilities of satellites to accurately capture MJO propagation. Modeling and forecasting efforts of the MJO will improve as the technology does as well. Satellites have already proven groundbreaking at expanding global observations in a variety of areas. The advancement of satellite and remote sending methods can only seek to enhance our current understanding and hopefully pave the way for the future.

Subdividing the MJO into primary and successive categories, based on propagation and strength, has proven invaluable in examining possible trigger mechanisms for MJO convection (Matthews, 2008). Successive MJO events are those that are preceded by sufficiently strong, coherent, preexisting MJO activity while primary MJOs are those not preceded by a period of coherent, preexisting MJO activity (Matthews, 2008). Although the MJO primarily initiates over the equatorial Indian Ocean (Straub, 2013; Webber et al., 2010, 2012), specific initiation mechanisms for initiating the MJO are less conclusive (Matthews, 2008). By definition, these primary MJO events are more uncommon than their successive counterparts and are inherently more difficult to pinpoint specific triggering mechanisms in a conclusive manner.

Despite being a highly researched topic, the MJO is still not fully understood. MJO initiation remains a subject of debate, as triggers have been proposed in both the atmosphere (Maloney & Hartmann, 1998; Wang et al., 2012; Zhao et al., 2013) and ocean (Webber et al., 2010, 2012) with substantial supporting evidence. From an oceanic perspective, Rossby waves have been shown to influence the initiation of MJO events by depressing the thermocline and thus increasing SST attributable to convective initiation (Oliver & Thompson, 2010), especially so for low-frequency primary events (Jensen et al., 2015; Webber et al., 2010, 2012). The arrival of a downwelling equatorial Rossby wave (ERW) would overall inhibit cold water entrainment from below and thus produce a region with higher SST favorable for convection (Jensen et al., 2015; McCreary, 1983; Shinoda et al., 2013). Additionally, it has been shown that air-sea interaction relative to MJO convection is stronger at lower frequencies over the Indian Ocean (Izumo et al., 2010). When SST is considered, model skill is improved and thus coupled air-sea processes are important to the propagation, and possibly growth, of the MJO (Woolnough et al., 2007). High SST acts to destabilize the lower atmosphere via anomalous surface fluxes, thus conditioning the lower atmosphere for convective growth. Evidence suggests that atmospheric boundary layer moisture convergence aids in the growth and propagation of the MJO by effectively refreshing atmospheric moisture availability that was depleted by the preceding convective period (Maloney & Hartmann, 1998), which further primes the Indian Ocean region for convective initiation to commence relative to the MJO. In addition, field campaigns such as the Cooperative Indian Ocean Experiment on Intraseasonal Variability in the year 2011 (CINDY)/Dynamics of the MJO (DYNAMO) have showed that strong moisture anomalies are paramount to initiating shallow convective cells that transition to deep convective systems (Bellenger et al., 2015) and that the western Indian Ocean remains a key initiation region from around 50–60°E (Li et al., 2015). The atmosphere has been shown to experience an intraseasonal increase in moist static energy (MSE) before an MJO event has reached a region with an abrupt discharge of MSE after and during the event's passing, suggesting that MSE can be used as a precursor signal for MJO initiation (Maloney, 2009; Sobel et al., 2014). In addition, MSE has been shown to be directly affected by increases in SST, further supporting the MJO and its initiation as a coupled air-sea phenomenon (Arnold et al., 2013). Spatial variability of SST has shown that the MJO geographically prefers high SST zones and its propagation speed therein (Lau & Shen, 1988).

Relationships with climate indices, such as the Indian Ocean Dipole (IOD) and the El Niño Southern Oscillation (ENSO), have been observed with the MJO. A negative IOD event is when the eastern Indian Ocean is anomalously warmer than in the west due to enhanced surface westerlies focusing warm waters

off the western Australian coast (Saji et al., 1999; Webster et al., 1999). Convective activity would be therefore supported over the eastern Indian Ocean and Maritime Continent regions during a negative IOD rather than positive due to the anomalous warm surface waters (Webster et al., 1999; Wilson et al., 2013). The opposite case would hold true for positive IOD events.

Although primarily focused over the Pacific Ocean, ENSO and the MJO have been shown to be very strongly interrelated (Hendon et al., 2007). ENSO activity can be influenced by the MJO through anomalous westerlies associated with the MJO's eastward propagation, which excite Kelvin waves that, through their associated currents, propagate warm water to the central and eastern Pacific Ocean (Tang & Yu, 2008). La Niña conditions exhibit anomalously warmer waters in the western Pacific in the Indo-Pacific Warm Pool, which would tend to support convective growth over this region (Moon et al., 2011). Conversely, El Niño exhibits a pattern of warmer waters over the central and eastern Pacific, which would tend to aid in convective growth further over the Pacific where the MJO typically begins to decay and could enhance MJO activity over and near North America (Moon et al., 2011). Studies have conventionally focused on the ENSO and MJO interaction over the Pacific Ocean rather than the Indian Ocean despite the latter being the initiation region of the MJO.

Strong air-sea coupling is associated with the MJO; thus, it becomes increasingly important to analyze ocean parameters in conjunction with the atmosphere so that a complete, holistic view of precursor MJO initiation conditions is considered. This study examines oceanic and atmospheric intraseasonal signals simultaneously to bridge the connection between ocean and atmosphere for primary MJO events to identify key similarities among primary MJO event precursor signals and to determine the difference in precursor signals between events during contrasting ENSO phases. As the MJO is strongly coupled, it is important to examine both the ocean and atmosphere simultaneously with regard to initiation conditions. While an increasingly large body of work exists as to MJO initiation, MJO primary event initiation, particularly under varying ENSO conditions, remains unclear, motivating this research. Two case studies of primary MJO events are presented on 20 September 2010 during a La Niña and 12 February 2015 during an El Niño in an effort to attribute primary MJO initiating mechanisms and their variability among ENSO phases. Broad-scale MJO variability during ENSO phases has been examined (Hendon et al., 2007; Tang & Yu, 2008) but less so have primary MJO events. The data and methods used in this paper are outlined in section 2. Section 3 presents the research results and pertinent discussion of two case study primary MJO events. Section 4 discusses overall conclusions presented in this study and what remains for future works.

2. Data and Methods

2.1. Atmospheric Data

The atmospheric data utilized in this study are the European Center for Medium Range Forecasts (ECMWF)'s ERA5 reanalysis product. ERA5 is composed of hourly data over 37 vertical pressure levels on a 0.25° horizontal grid and is available from 1979 through present (Hersbach et al., 2019). Although many distinct variables are available in the ERA5, temperature (T), specific humidity (q), and horizontal (zonal, u; meridional, v) winds are used for studying precursor MJO initiation conditions over the equatorial Indian Ocean. ERA5 is the successor to the discontinued ERA-Interim, which has been used previously and shown reliable at monitoring the MJO and its moisture budget (Sobel et al., 2014). To observe the convective signal of the MJO, National Oceanic and Atmospheric Administration Climate Prediction Center (NOAA-CPC)'s outgoing longwave radiation (OLR; Liebmann & Smith, 1996) is used. The OLR data are presented on a daily 0.25° grid and available from 1974 through 2018. NOAA-CPC's OLR has been shown to accurately capture the spatiotemporal propagation of the MJO's eight phases (Hendon et al., 2007; Shoup et al., 2019).

2.2. Oceanic Data

SST from the Advanced Very High Resolution Radiometer (AVHRR) is used for the intraseasonal SST signal relative to the MJO. The AVHRR optimally interpolated (OI) SST V2 High Resolution product, provided by NOAA, is presented on a daily 0.25° grid and available from September 1981 through present (Reynolds et al., 2007). Previous studies have used AVHRR SST in the Indian Ocean to study intraseasonal oscillations thus proving its reliability (Roman-Stork et al., 2019). Since the AVHRR OI SST product has some cloud contamination, the Group for High Resolution Sea Surface Temperature (GHRSST) Level 4 Canadian

Meteorological Center (CMC) 0.2° grid product (Chao et al., 2009) is also used when available for comparison purposes during September 1991 through 18 March 2017. MJO-related precipitation has been previously linked with SST from GHRSST (Carbone & Li, 2015) thus supporting its viability. Furthermore, GHRSST Level 4 CMC 0.2° is a blended product consisting of ERS-1 and ERS-2, Envisat, AVHRR from the NOAA series satellites (NOAA-16, 17, 18, and 19), AMSR-E, Windsat, and in situ SST observations. Blended altimetric absolute dynamic topography (ADT) from the Copernicus Marine Environment Monitoring Service (CMEMS, marine.copernicus.eu) is also used and is provided on a daily 0.25° grid available from 1993 through 2018 (Ducet et al., 2000; Le Traon et al., 1998). ADT from satellite altimetry is functionally similar to that of model-derived sea surface height (SSH) and is used to show the possible arrival of oceanic downwelling ERWs.

2.3. MJO and Climate Indices

The MJO has can be examined through the use of empirical indices. One such index is the Real-Time Multivariate MJO Index (RMMI), which utilizes synchronous circulation and convective signals (Wheeler & Hendon, 2004). The RMMI used for the purposes of this study is provided by the Australian Government Bureau of Meteorology (AGBoM). The AGBoM's RMMI product, which is calculated using the methods of Wheeler and Hendon (2004), is available in daily format from 1974 through present and provides daily MJO amplitude, phase number, and RMM components (RMM1 and RMM2). Other indices, such as the OLR MJO Index (OMI), have also been employed to study MJO convective spatiotemporal evolution (Kiladis et al., 2014). Given that the focus of this study is precursor signals relative to MJO convective initiation, we utilize both the RMMI and OMI when considering primary MJO events while focusing primarily on the OMI phase signals. The RMMI has been used to identify primary MJO events previously (Shoup et al., 2019; Straub, 2013), but the OMI is better suited for the study of the evolution of individual MJO events (Kiladis et al., 2014) and will thus be focused upon as the index of choice in this study, especially pertaining to the initiation of primary MJO events.

In addition to the RMMI and OMI MJO indices, this study also employs the Oceanic Niño Index (ONI), which is based on 3-month running means of SST anomalies (SSTA) in the Niño 3.4 region (5°S–5°N, 120–170°W) to describe the ENSO. ONI values exceeding ± 0.5°C indicate the presence of an El Niño (warm phase) and La Niña (cold phase). The final index being used is the Dipole Mode Index (DMI) to describe the IOD (DMI; Saji et al., 1999). The DMI is calculated as the anomalous gradient between a western (10°S–10°N, 50–70°E) and eastern (10°S–equator, 90–110°E) Indian Ocean box averaged SSTA. The DMI in this study was manually calculated in daily format from September 1981 through 2018 using AVHRR OI SST V2. A positive (negative) IOD event is present when the western (eastern) Indian Ocean anomaly exceeds the eastern (western) by greater than 1 temporal standard deviation (Wilson et al., 2013).

2.4. Methods

The identification of primary MJO events is done in a similar manner to that of Matthews (2008) using OLR and MJO indices as a reference for detection capabilities. By observing the spatiotemporal evolution of the OLR signal, convective peaks can be observed over the Indian Ocean as a transition from positive to negative OLR anomalies. If the convective peak is not preceded by coherent eastward propagating low OLR, then the event is said to be a primary MJO (Matthews, 2008).

To examine the moisture profile conducive to MJO initiation, moisture flux convergence (MFC) is calculated by using the ERA5 variables. Horizontal MFC is derived from water vapor conservation budget, expressed as $Dq/Dt = S$, where S represents sources and sinks of atmospheric water vapor (Banacos & Schultz, 2005), which is shown as

$$E - P = \frac{\partial q}{\partial t} + \nabla \cdot q\overrightarrow{V_H} + \frac{d}{dp}(q\omega). \tag{1}$$

Specific humidity is represented by q, and omega (ω) is the vertical velocity in pressure coordinates. $\overrightarrow{V}_H$ is the horizontal wind vector (u, v). Horizontal MFC is therefore defined as

$$MFC = -\nabla \cdot q\overrightarrow{V_H} = -u\frac{\partial q}{\partial x} - v\frac{\partial q}{\partial y} - q\left(\frac{du}{dx} + \frac{dv}{dy}\right). \tag{2}$$

The first two terms on the right side of equation 2 ($-u\frac{\partial q}{\partial x} - v\frac{\partial q}{\partial y}$) represent moisture advection; the second set of terms in equation 2 ($-q\left(\frac{du}{dx} + \frac{dv}{dy}\right)$) denotes moisture transport due to horizontal convergence of mass.

The transfer of moisture into and out of a system also alters the vertical distribution of MSE (Neelin & Held, 1987). MSE can be used to diagnose if a given region in the atmosphere is conducive to instability relative to convective initiation and is expressed as

$$MSE = C_{pd}T + gz + L_v q, \tag{3}$$

where C_{pd} is the specific heat capacity of dry air at constant pressure, L_v is the latent heat of vaporization of water at 0°C, and g is the gravitational acceleration constant. The first term represents the thermal energy within an air parcel, and the third term represents the latent heat energy within that same parcel if all available moisture were to instantaneously condense out. The second term (gz) represents parcel potential energy (geopotential) at a given altitude. To examine the full atmospheric profile, MSE can be vertically integrated and mass weighted between two layers, which can be expressed in integral form as

$$\frac{1}{g}\int_{P_u}^{P_L} MSE(P)\, dP. \tag{4}$$

P_L denotes the pressure at the lower level (the higher-pressure value) and P_u the upper level (the lower-pressure value) of the layer. $MSE(P)$ indicates the MSE at a given pressure level P, and dP is the pressure difference between the lower and upper levels in pascals (pa).

The MJO is typically observed over 30-90-day periods but has been observed at a broader range of 20–100 days. As such, a fourth-order Butterworth bandpass filter across the 20-100-day period, similarly to that of Matthews (2008), is used. The filter is further applied forward and backward through time to mitigate possible edge effects, which also acts to detrend the data. In addition, the filter is not significantly affected by removing the seasonal cycle. This filter is applied to oceanic and atmospheric parameters simultaneously to observe coupled air-sea effects interaction MJO timescales and diagnose possible concurrent trigger mechanisms. Anomalies are calculated by removing the annual mean. In addition, the western half of the Indian Ocean (40–75°E) has been proposed as the key initiating region for MJO convection (Webber et al., 2012). This longitude range was further broken down into three smaller regions (40–50°E, 52.5–62.5°E, and 65–75°E) in order to examine variability over a smaller scale. This was done to prevent variables from being smoothed out over a much larger scale.

Composite analysis was also performed over the same strong MJO years identified in Shoup et al. (2019). These events were originally identified using the RMMI, which, due to the inherent noise level, generally provides a less accurate initiation signal compared to exclusively OLR-based indices. As such, the primary event initiation dates originally defined by Shoup et al. (2019) were adjusted to reflect the usage of the OMI, although the RMMI is still presented for comparison purposes. The initiation of these events was determined to be the first day in the OMI in which the amplitude exceeded a value of 1.0. If the OMI amplitude remained between 0.8 and 1.0 while consistently rotating counterclockwise, through at least four consecutive phases, then the event was determined to persist, where event dissipation was determined on the day in which the OMI fell below 0.8. An important note, however, is that the initiation of primary MJO events using an index is subjective and defining initiation characteristics have varied across studies (Kiladis et al., 2014; Matthews, 2008; Straub, 2013). The two case study events were chosen due to synchronicity with prevailing ENSO phases such that contributing variability from El Niño and La Niña conditions can be examined. Two case study primary MJO events were then examined with initiation on 20 September 2010 and 12 February 2015 and their relative oceanic and atmospheric signals preceding peak convection compared to composites of the identified primary MJO events in the strong MJO years used in Shoup et al. (2019) of 2010, 2012, 2015, and 2017 (Table 1).

Table 1
Primary MJO Initiation Dates as Found From the OMI for 2010, 2012, 2015, and 2017, Following the Methodology of Shoup et al. (2019)

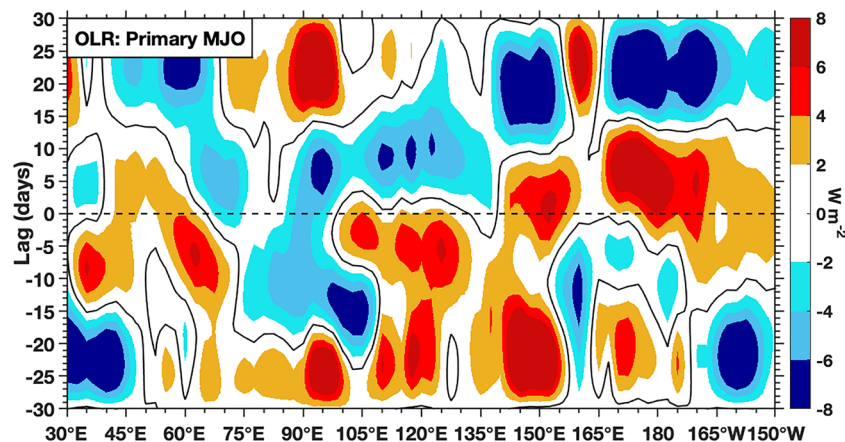| Year	Initiation date
2010	20 September
	11 November
2012	2 January
	26 May
2015	12 February
	29 May
	11 December
2017	14 October
	20 November

3. Results and Discussion

3.1. Primary MJO Convective Signal

The composite OLR signal of all identified primary MJO events is examined first (Figure 1), where composites were constructed based on nine events between 2010 and 2017 (Table 1). The signal preceding the composite initiation day does not represent that of a coherently organized MJO event. This pattern then quickly develops into a more coherent signal at Day 0 over the Indian Ocean before continually propagating eastward as a band of negative OLR anomalies, which would indicate enhanced MJO convection. The red spot, indicating suppressed MJO activity, from Lag Days 20–30 between 150°E and 165°E is likely an artifact of the compositing technique exhibiting that MJO events typically decay in the Pacific Ocean, although not all events will decay in such a manner and may persist during circumnavigation.

The development of the two primary MJO events in question can be seen clearly through the time-longitude diagrams of their respective intraseasonal OLR signals (Figures 2 and 3). The development of the 2010 primary MJO convective signal can be observed through the generation of negative OLR anomalies, which are indicative of strong, deep cloud formation associated with the MJO (Figure 2). No coherent pattern of eastward propagating negative OLR anomalies that would be indicative of a well-developed MJO is observed to precede the peak convection centered on 20 September 2010 (Figure 1). The convection then organizes into a coherently eastward propagating signal that would be typical with that of an MJO event. The MJO indices also show the development of the primary MJO signal, albeit much more clearly in the OMI. The OMI shows that a coherent, sufficiently strong eastward propagating convective signal is lacking in much of September that then develops into one that is more prominent toward the middle and tail-end of September. Most of the RMMI signal surrounding 20 September 2010 is incoherent and not resembling a developed MJO until nearly 2 weeks later than the OMI in early October. The MJO signal in the RMMI is not of sufficient strength to be considered a primary MJO event until at least 2 October (Shoup et al., 2019) while the OMI signal has already been established, which further demonstrates the discrepancies between the two MJO indices. The OMI in 2010 indicates that the initiation was over the Indian Ocean, which further aligns with the observed OLR pattern in Figure 2a.

The primary event identified on 12 February 2015 exhibits a similar spatial pattern to that of the 2010 event (Figure 3). The convective peak is observed over 75–90°E, much like 20 September 2010, while preceded by incoherent intraseasonal OLR signals. The convective peak then propagates eastward, where a clear alternating between negative (enhanced convection) and positive (suppressed convection) is observed, thus demonstrating the alternating convective phases of the MJO. The RMMI in January through the first week

Figure 1. Lag-composite time-longitude plot of filtered outgoing longwave radiation (OLR; W m^{-2}) of primary MJO events (Table 1) averaged over 10°S to 10°N. The black dashed line denotes the composite initiation day. The solid black contour denotes the 0 W m^{-2} contour.
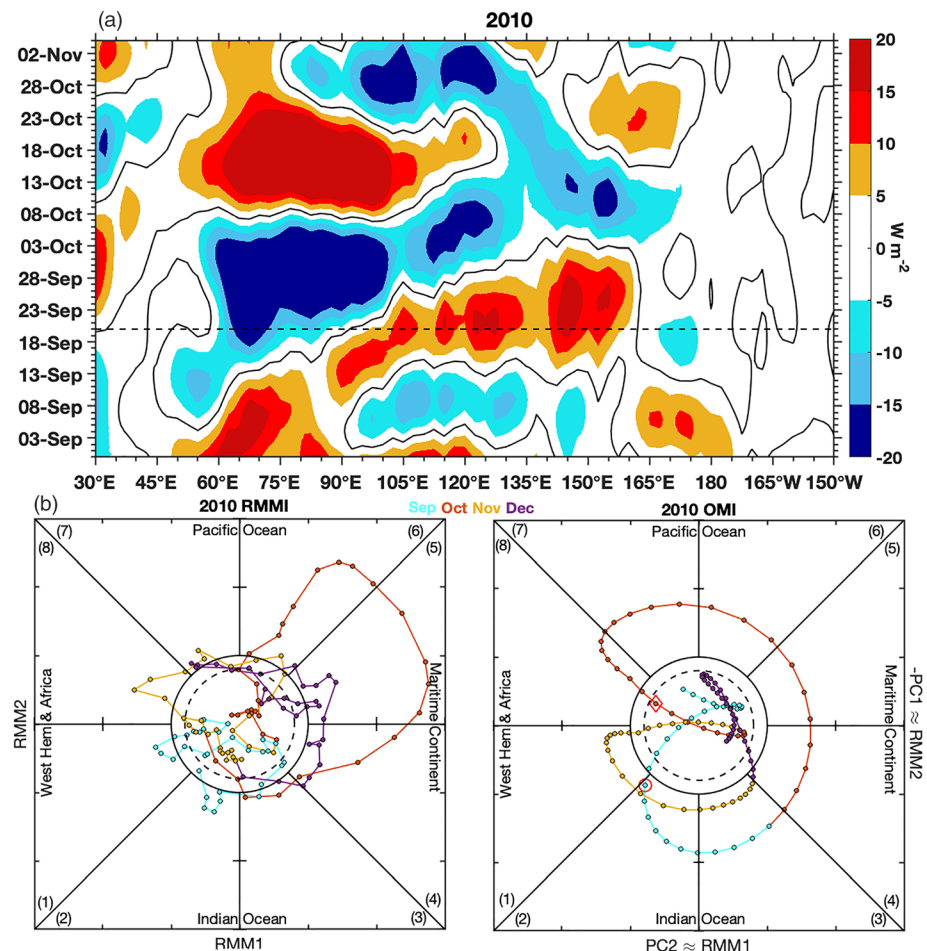
Figure 2. (a) 20-100-day filtered latitudinally averaged (10°S–10°N) Hovmöller diagram of OLR anomalies (W m^{-2}) with (b) RMMI (left) and OMI (right) phase diagrams relative to the 20 September 2010 primary MJO initiation. The black dashed line in (a) denotes 20 September. The solid (dashed) circles in (b) denote amplitude 1.0 (0.8) in the RMMI and OMI. The red circle (diamond) in the OMI represents initiation (dissipation) of the event.

of February exhibits incoherent propagation that develops into clear eastward propagation for middle to late February and beyond through March. The RMMI would suggest that the MJO signal for this event is not sufficient enough to be considered a well-developed MJO event, let alone a primary MJO, until at least 3 March (Shoup et al., 2019), which is nearly 3 weeks later that the signal evident in OLR and the OMI. The OMI captures this primary MJO event more clearly than the RMMI by exhibiting a more coherent sense of eastward propagation pre- and post-initiation, suggesting that the OMI is more effective at capturing the convective signal relative to MJO initiation than the RMMI (Kiladis et al., 2014). Overall, the OMI has exhibited a stronger ability to capture coherent MJO eastward propagation for the two primary MJO events and remains the more reliable of the two in monitoring MJO variability, although the RMMI still provides accurate broad-scale indications MJO propagation (Kiladis et al., 2014).

3.2. Existing ENSO and IOD Conditions

The IOD and ENSO can influence the Indian Ocean and thus the MJO in prominent ways. The IOD has been shown to heavily influence the Indian Monsoon System through anomalous surface fluxes attributable to changes in SST across the basin (Ashok et al., 2001). Evidence also suggests that the IOD MJO activity, namely, propagation strength, is enhanced during a negative IOD phase over the Maritime Continent and Indian Ocean but suppressed during a positive IOD event (Wilson et al., 2013).

The DMI preceding the 2010 primary event was sufficiently negative from September through November indicating the presence of a negative IOD phase (Figure 4). The negative IOD conditions of 2010 would
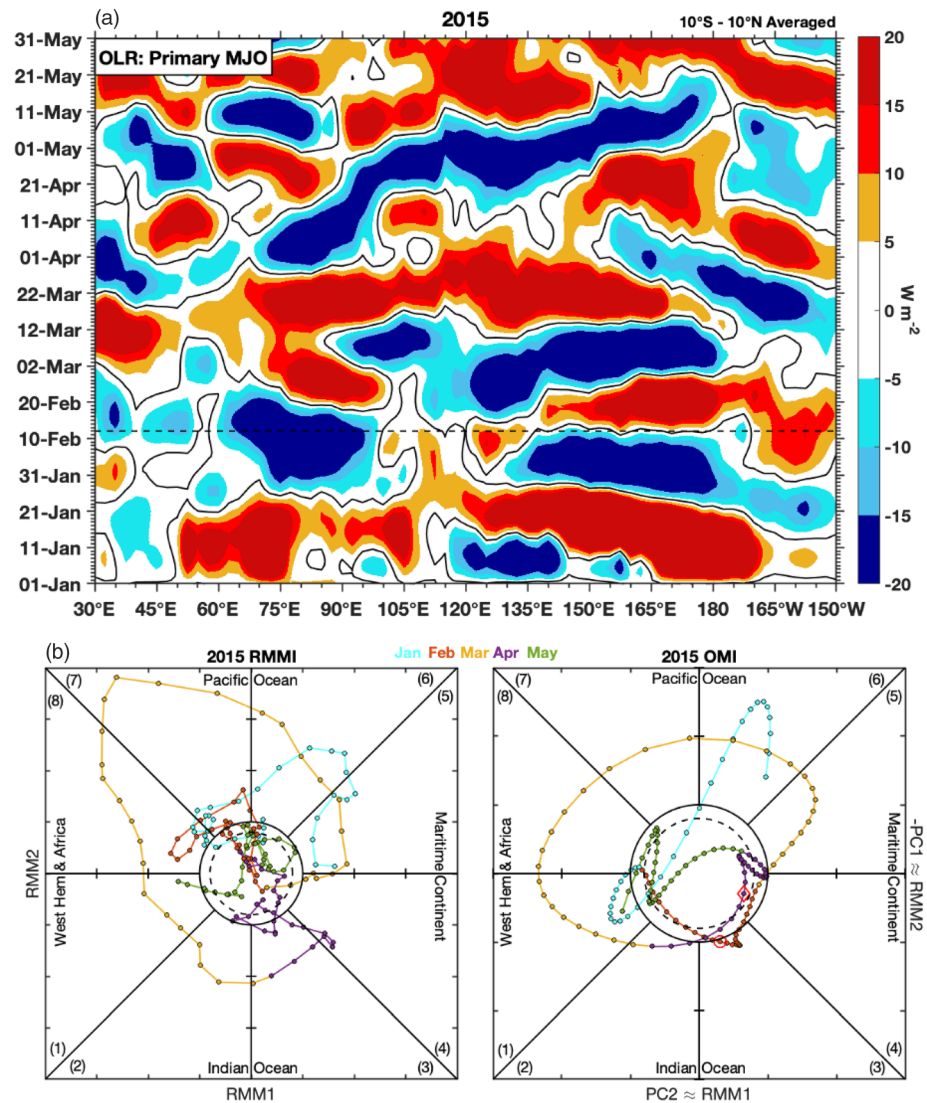
Figure 3. As in Figure 2 but for January through May of 2015. The black dashed line denotes 12 February 2015. The solid (dashed) circles in (b) denote amplitude 1.0 (0.8) in the RMMI and OMI. The red circle (diamond) in the OMI represents initiation (dissipation) of the event.

act to enhance convective activity over the Maritime Continent, which can be observed in Figure 1 as peak negative OLR anomalies persisting around this region. The IOD in 2010, however, was steadily increasing to a more positive value, so it is possible that the effects of a sufficiently developed negative IOD are masked by this gradual transition to IOD neutral conditions. The primary MJO event of 2015 maintains a negative DMI value, but its value is not sufficient to be considered a well-developed negative IOD event. Conditions at the time are thus considered IOD neutral since the DMI value surrounding the primary MJO event's initiation was within the 1 standard deviation threshold (Saji et al., 1999). The OLR anomalies and MJO index phase diagrams of Figure 2 show that sufficiently strong MJO signals are maintained over this region, which is to be expected from the Maritime Continent region maintaining naturally warmer waters than the western Indian Ocean on average due to the presence of the Indo-Pacific Warm Pool.

The 2010 primary MJO is concurrent with strong negative values in the ONI indicative with a strong La Niña event. The western Pacific exhibits a strong convective MJO propagation (Figure 2) over the Maritime Continent and Indo-Pacific Warm Pool region; thus, the warm waters of the western Pacific Ocean would act to maintain this convection. The convection of the 2010 primary MJO decays leading into late October and November of 2010, which coincides with strong La Niña conditions over the Pacific Ocean (Figures 4
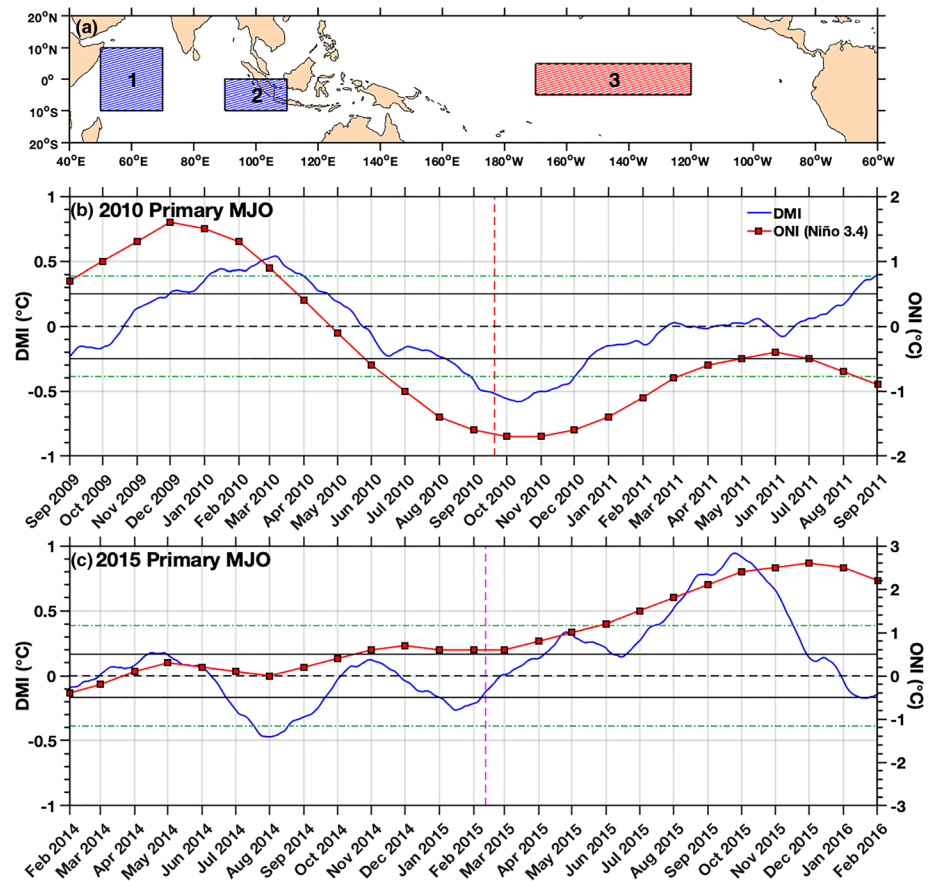
Figure 4. (a) DMI (blue) and ONI (red) reference regions. (b) Monthly ONI (ref, right axis) and 100-day smoothed DMI (blue, left axis) for 2009 through 2011. The black solid lines denote the ±0.5°C threshold for ENSO events. The green dashed lines denote ±1 standard deviation threshold in the DMI (~ ±0.4°C). (c) As in (b) but for 2015 through 2016. The red (magenta) dashed lines denote 20 September 2010 (12 February 2015).

and 5). The anomalous cold waters of the eastern Pacific Ocean would act to suppress convective growth associated with the MJO (Figure 5), which can be seen as the negative OLR anomalies across the propagation path in Figure 2 weaken and turn positive approaching the international date line before dissipating over the central and eastern Pacific Ocean. The anomalous upwelling along the eastern Pacific
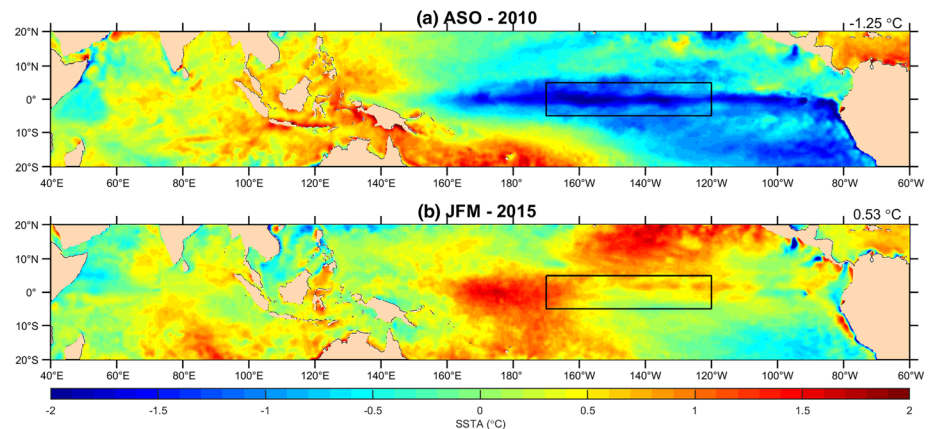
Figure 5. Seasonally averaged SSTA (°C) for (a) August–March (ASO) 2010 and (b) January–March (JFM) 2015 using AVHRR OI SST. The black box denotes the Niño 3.4 reference region (5°S to 5°N, 120–170°W). Average SSTA in the Niño 3.4 reference region is indicated in the top right of each panel.
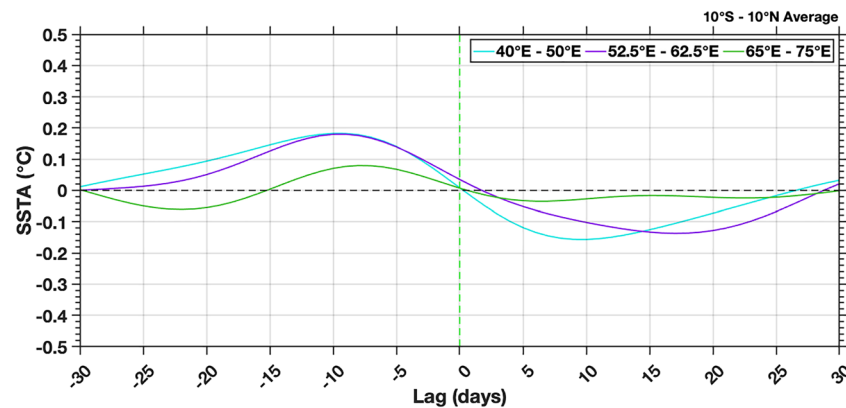
Figure 6. Time-lag composite of 20- to 100-day filtered box averaged sea surface temperature anomalies (SSTA, °C) from AVHRR OI SST averaged over 10°S to 10°N. The green dashed line denotes the composite initiation day.

Ocean due to the strong La Niña would act to continually suppress MJO convection by a shallowing of the thermocline that would reduce OHC and, respectively, convective activity. In addition, the strong La Niña would enhance the trade winds and suppress equatorial Kelvin waves (EKWs) from transporting warm waters to the eastern Pacific, effectively cutting off the warm SST fuel supply for MJO convection.

2015 was a remarkable year for ENSO, as the 2015/2016 El Niño was one of the strongest events on record, similar to that of the 1982/1983 and 1997/1998 events (Santoso et al., 2017). The ONI at the time surpasses the 0.5°C threshold to be considered an El Niño event when this primary MJO has initiated (Figure 4), although the El Niño was still in the process of developing. This can be seen in Figure 5, where high SSTA in the Niño 3.4 region shows El Niño conditions. The El Niño was strengthening rapidly while this MJO was propagating over the central and eastern Pacific Ocean, which would act to enhance the propagation strength and capabilities of this MJO. Interestingly, it has been proposed that this primary MJO event in question actually influenced the onset of the 2015/2016 El Niño by exciting westerly wind bursts that force downwelling Kelvin waves in early March over the western Pacific (Hong et al., 2017). Figure 3 shows that the MJO and its convective signal was, in fact, present over the western Pacific Ocean and Maritime Continent during this time. Additionally, the convective signal in Figure 3 projects across the Pacific Ocean to the international date line and beyond quite strongly, where the negative OLR band recirculates back across the Indian and Pacific oceans for a persistent, clear circumnavigating MJO signal that remains strong in both the RMMI and OMI. The RMMI and OMI support this, as the indices' values are consistently of sufficient strength and of continual eastward propagation (counterclockwise rotation around the phase diagram). The RMMI experiences a peak amplitude of 4.62 over the Pacific Ocean on 16 March 2015, which coincides with sufficiently strong El Niño conditions in the ONI. This suggests that the predominant El Niño conditions may have contributed to the strong, persistent propagation across the Pacific Ocean and beyond where the MJO would typically begin to weaken due to strong thermocline deepening induced during El Niño conditions, which would suppress upwelling and therefore increase OHC and convective activity accordingly. The Indo-Pacific Warm Pool plays a crucial role in global climate (De Deckker, 2016) and ENSO dynamics (Picaut et al., 1994), and the weakening of the trade winds over the western Pacific Ocean would allow for EKWs to excite and transport Indo-Pacific Warm Pool waters to the central and eastern Pacific Ocean that the MJO could then utilize as fuel for deep convection.

### 3.3. Intraseasonal Ocean Variability

In this section we examine the intraseasonal variability of coupled air-sea parameters as it pertains to the initiation of the two MJO events presented. It has been previously shown that high SST actively contributes to convective propagation and initiation of the MJO (Rydbeck & Jensen, 2017) through anomalous surface fluxes. Figure 6 shows that SST peaks across the western Indian Ocean upward of 10 days prior to the initiation that promptly decreases during and after event propagation. This affirms that SST preceded convective initiation of the MJO and actively contributes to its initiation, which is consistent with previous studies (Rydbeck & Jensen, 2017).
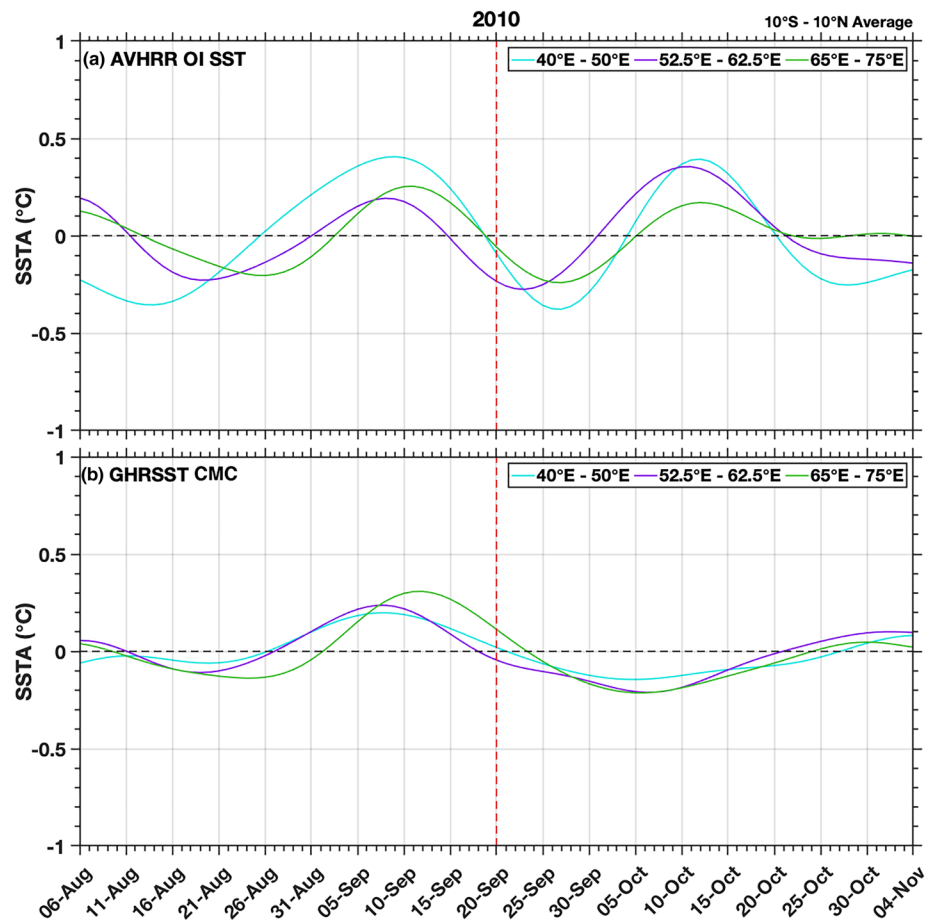
Figure 7. As in Figure 6 but for (a) AVHRR OI SST and (b) GHRSST CMC SST. The red dashed line denotes 20 September 2010.

The SST signal associated with the 2010 primary MJO event (Figure 7) exhibits a pattern similar to that of the composite of all events. SST peaks in the western Indian Ocean about 10 days prior to convective initiation for AVHRR IO SST with the easternmost range (65–75°E) peaking just days after. This indicates that downstream SST is maintaining high enough to actively contribute to MJO propagation and development. The SST from CMC GHRSST exhibits a similar timing to that of AVHRR IO SST but at different magnitudes, especially over the westernmost range (40–50°E). The SST signal of AVHRR IO SST at this range is double that of the CMC GHRSST signal at the same time, which may be the product of the blended nature of CMC GHRSST and the cloud contamination in AVHRR IO SST. Regardless, both products exhibit the same general idea that SST should be peaking before the MJO event has initiated and then decrease during and after its propagation. The 2015 primary event also exhibits a similar pattern of high AVHRR IO SST preceding convective initiation, but the signal remains of generally higher magnitude to that of 2010 and is temporally closer to that of initiation than 2010 (Figure 8). The CMC GHRSST signal in 2015 is not consistent with what can be expected preceding a primary MJO event. This is likely due to the blended nature of the CMC GHRSST product. Overall, the AVHRR IO SST product seems more reliable at monitoring pre-initiation SST than CMC GHRSST.

The 2010 primary MJO event was synchronous with a La Niña event while the 2015 was with an El Niño. A prevailing La Niña generally correlates to an overall cooling effect over the Indian Ocean (Kug & Kang, 2006) while an El Niño correlates to a warmer Indian Ocean (Ashok et al., 2004). This would explain why the SST signals surrounding the initiation of the 12 February 2015 event are of higher magnitude than the 2010 event. In addition, the spatial distribution of peak SSTA over the Indian Ocean during an El Niño is focused over the region around 60°E (Ashok et al., 2004), which is expressed here for the 2015 primary MJO
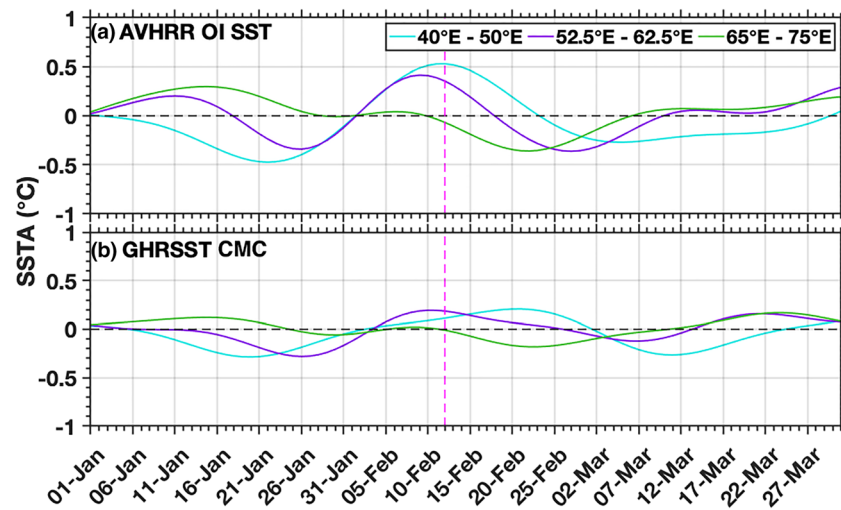
**Figure 8.** As in Figure 7 but for 2015. The magenta dashed line denotes 12 February 2015.

(Figure 8). The timing of the SST signal relative to the initiation of the 2015 MJO can be likely attributed to the fact that, at the time, the El Niño was in the process of development and has not yet come close to its peak, so SST would have undergone a transition period from the cold influence of La Niña/neutral to the warmer El Niño conditions.

Primary MJO events have also been shown to be preceded by the arrival of downwelling ERWs primarily on the low-frequency range (Webber et al., 2010, 2012). Looking at the composite ADT field surrounding the initiation of primary events (Figure 9) does not seem to initially support this idea. Figure 9 shows the ADT field at the latitudes 4°S and 4°N, which were chosen as the central axis of ERW propagation based on the Rossby radius of deformation for this region of 4–5° (Chelton et al., 2003). Since it is functionally similar to that of model-derived SSH, ADT can be used to detect ocean waves in a similar manner. Positive anomalies in the sea surface would be indicative of downwelling Rossby wave activity. What is observed here, however, is that positive values of ADT are present leading up to the initiation of the primary MJO events but not in a manner fashion that would indicate coherent westward ERW propagation that would be expected. The forcing of these ERWs is highly variable over space and time in the Indian Ocean (Webber et al., 2010, 2012), which can make studying these low-frequency waves difficult in a composite sense. A more coherent picture, however, is observed when examining the individual events separately.
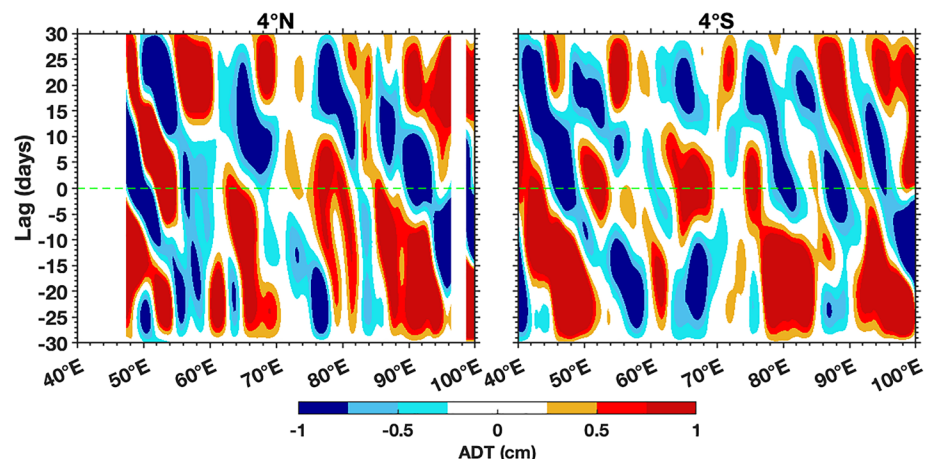
Figure 9. Hovmöller diagram of composite absolute dynamic topography (ADT, cm) from CMEMS at (left) 4°N and (right) 4°S. The green dashed line denotes the composite initiation day of the primary MJO events.
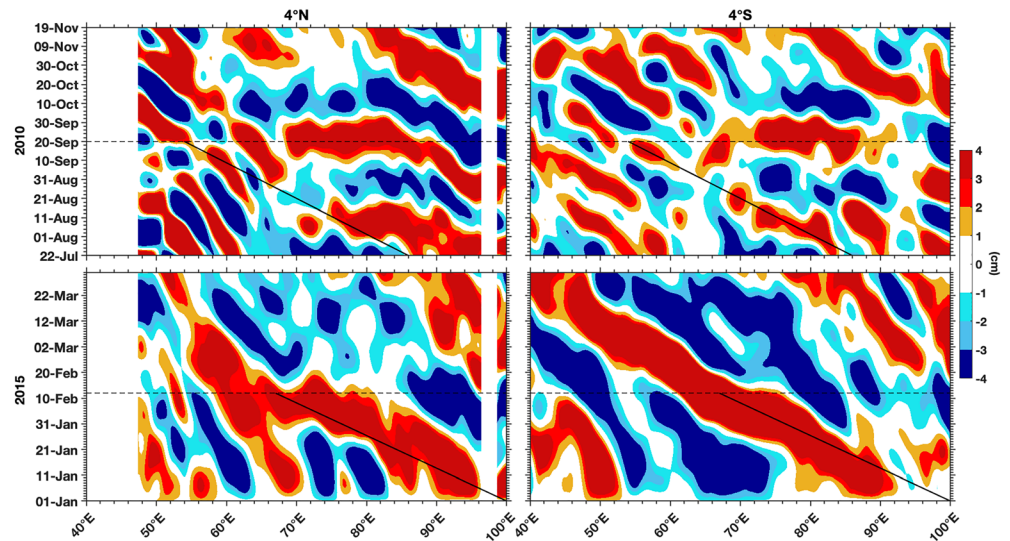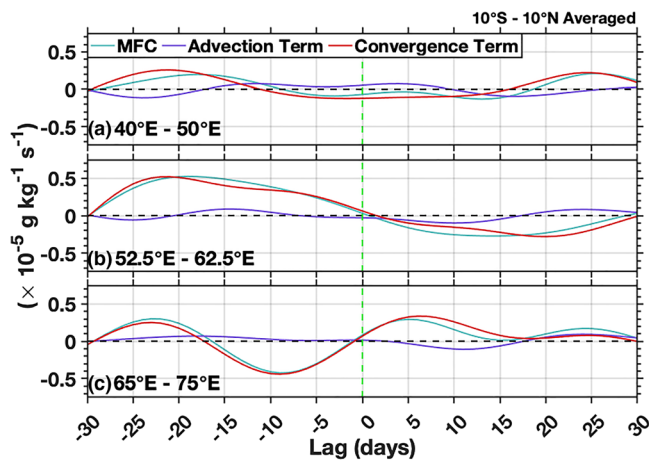
Figure 10. CMEMS ADT anomaly (ADTA, cm) at (left) 4°N for (top) 2010 and (bottom) 2015 and at (right) 4°S for (top) 2010 and (bottom) 2015. The black dashed line denotes 20 September 2010 and 12 February 2015 initiation days, respectively. The solid black line denotes the westward propagation of oceanic equatorial Rossby waves (ERWs).

A clear ERW can be observed to propagate along 4°S in 2015 leading up to the initiation of the 2015 primary MJO with an estimated speed of 0.98 m s^{-1} (33° of longitude, 67–100°E, covered over 43 days leading up to 12 February). This estimated phase speed is relatively high but within the realm of possibility for Rossby wave phase speed at this latitude (Chelton et al., 1998). While not as pronounced as the ERW at 4°S, a paired ERW at 4°N is observed at the same time and along the same path as its 4°S counterpart.

A pair of ERWs are observed in 2010, like those in 2015, with their arrivals coinciding with the development of the primary MJO event (Figure 10). The phase speed for these ERWs is estimated at 0.68 m s^{-1} (32° of longitude, 54–86°E, covered over 60 days leading up to 20 September 2010), which is consistent with possible ERW phase speeds at this latitude (Chelton et al., 1998). The western half of the Indian Ocean must sense the arrival of the ERW in order for the initiation contribution of ERWs to be considered (Webber et al., 2012), and these two primary MJO events certainly see the arrival of such waves. This suggests that El Niño events may lead to generally stronger ERW activity over the Indian Ocean while a La Niña weakens the signal.

Being that a La Niña is an enhancement of normal conditions, this can help explain why the composite ADT signal is incoherent in Figure 9 since El Niño conditions are the exception rather than the norm.

3.4. Intraseasonal Atmospheric Variability

With respect to atmospheric signal of the MJO, the 850-hPa level is commonly seen as a key level for activity. When observing the lower atmosphere, the 850-hPa level is seen to exhibit distinct increases in MFC prior to initiation that quickly transitions into negative values during and after the MJO has propagated through (Wang, 1988), specifically from 52.5–62.5°E (Figure 11). This means that moisture intrusion into the lower troposphere is being observed, which is widely considered to be necessary for initiation of shallow convection that would then translate to the development of deep convection associated with the MJO.


Figure 11. Time-lag composite of 20- to 100-day band-pass filtered, box averaged 850-hPa MFC for (a) 40–50°E, (b) 52.5–62.5°E, and (c) 65–75°E over 10°S to 10°N. The green dashed line denotes the composite initiation day of the primary MJO events.

The MFC signals associated with the 2010 and 2015 primary MJO event broadly follow this same composite MJO trend (Figure 12). The initiation of both events is accompanied by spikes in MFC but specifically dominated by the convergence term of the total MFC while the advection term is negative. Being that the events have begun to coherently form, the
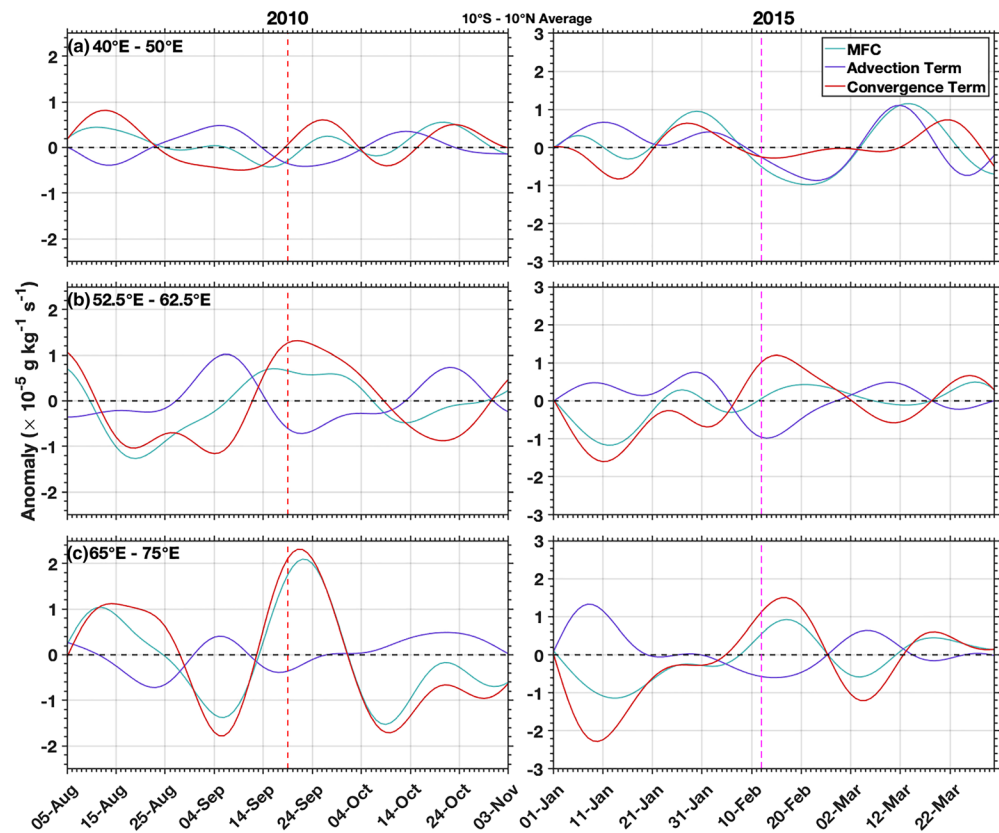
Figure 12. As in Figure 11 but for (left) 2010 and (right) 2015. The red and magenta dashed lines denote the initiation on 20 September 2010 and 12 February 2015, respectively.

prevailing circulation pattern of an active MJO phase would cause a general convergence of moisture while the prevailing MJO westerlies would advect moisture away. The key regions for spikes in MFC cover the 52.5–62.5°E and 65–75°E ranges, but this does not appear to be immediately synchronous with SST. The warm SSTs may help to destabilize the lower atmosphere such that convection is favored, but if the MJO circulation is not present, then convection is less likely to strongly develop. Regardless, high SST is observed around the same peaks of MFC and force lower atmospheric convergence (Marshall et al., 2008), thus indicating that low-level moisture convergence is likely preconditioning the lower troposphere for deep convection.

The differences between the 2010 and 2015 MFC signals relative to their MJO initiation are more striking by looking at the 52.5–62.5°E and 65–75°E ranges. The moisture advection term of MFC is nearly identical between the two events from 52.5–62.5°E and 65–75°E while the key difference is in the convergence term being higher during the 2010 event initiation. This suggests that, in spite on the colder Indian Ocean temperatures that would be less favorable or convection, the La Niña conditions favored stronger convergence over this longitude range that would lead to an overall stronger MFC signal conducive to MJO initiation.

As 850-hPa MFC would be an indicator of low-level convective priming, column MSE would be an indicator of the full atmosphere. The key regions for peak composite MSE lie from the westernmost boxes of 40–50°E and 52.5–62.5°E (Figure 13). These two boxes indicate a pattern typical with that of a recharge-discharge paradigm that MSE increases prior to MJO initiation but rapidly discharges as the event develops and matures (Kemball-Cook & Weare, 2001; Sobel et al., 2014). This peak in MSE also overlaps with the timing of peak SST in Figure 6, as warm SSTs would act to destabilize and moisten the atmosphere such that convection is favored, which affirms the coupling of SST to MSE (Arnold et al., 2013). The 65–75°E domain rather exhibits a pattern that would suggest, being downstream from the peak MSE, this region is still being primed to favor MJO convection such that MSE is high as it propagates through and convection can persist.
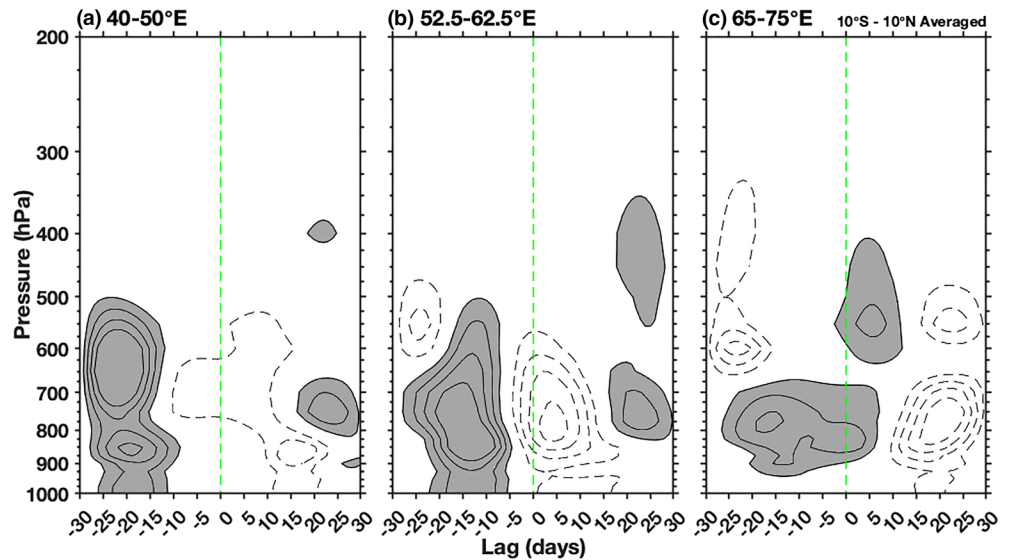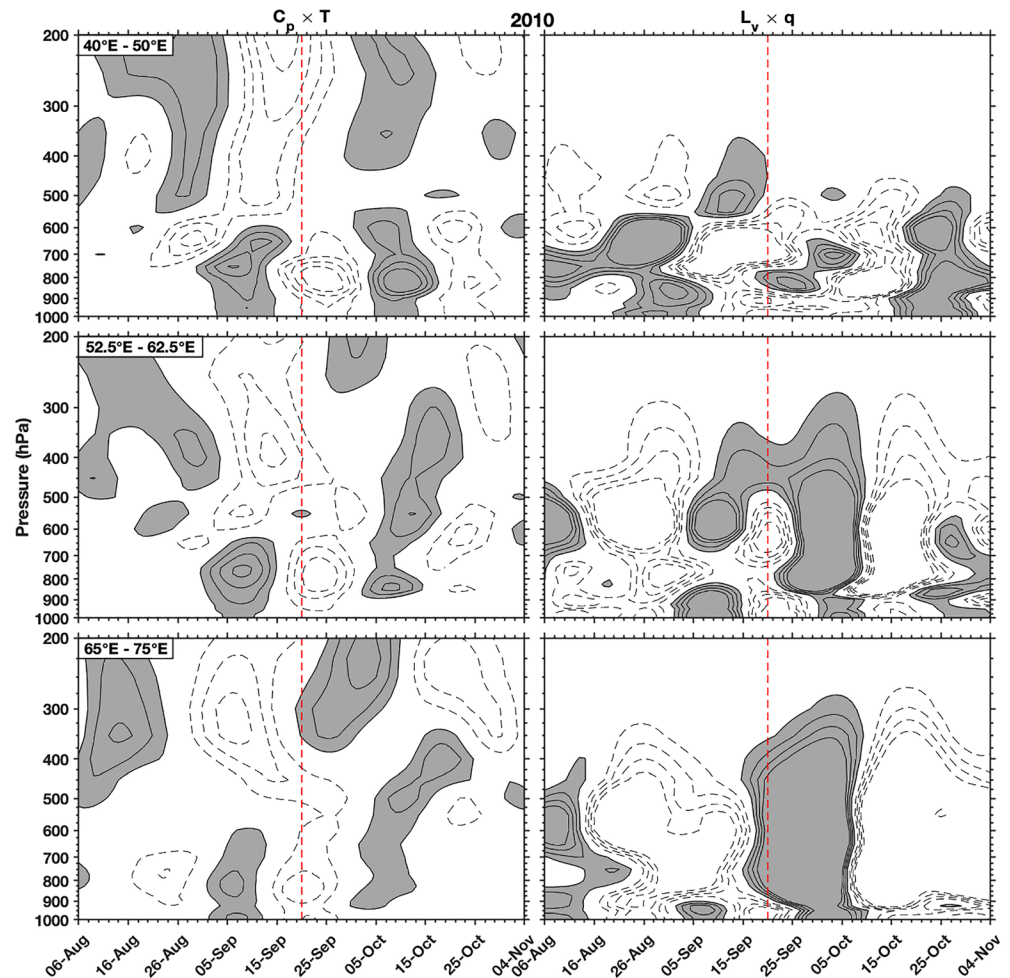
Figure 13. Box averaged vertical distribution of composite MSE (J kg^{-1}) over all identified MJO events. Positive (negative) values are shaded (non-shaded) gray in solid (dashed) contours. The green dashed line denotes the composite MJO initiation day. The zero contour is omitted, and the contour interval is 250 J kg^{-1}. The pressure axis is log$_{10}$ scaled to reflect nonlinear atmospheric pressure scaling.

Breaking apart the full MSE into its respective terms (Figure 14) can provide a more holistic indication of factors contributing to MJO initiation. As moisture is crucial in convective growth, Figure 14 shows that the effects of latent heat energy, represented by $L_v q$, dominate the full MSE profile. Moisture, however, is not enough to initiate convection on its own. Atmospheric destabilization takes place in the form of midtropospheric cooling, which drags the temperature profile down such that any rising air is more likely to remain unstable and form deep convective pockets.

The MSE component profiles of 2010 (Figure 15) and 2015 (Figure 16) show a general similarity to the composite profile. For the 2010 primary MJO, a weak low-level positive moist static energy anomaly (MSEA) is
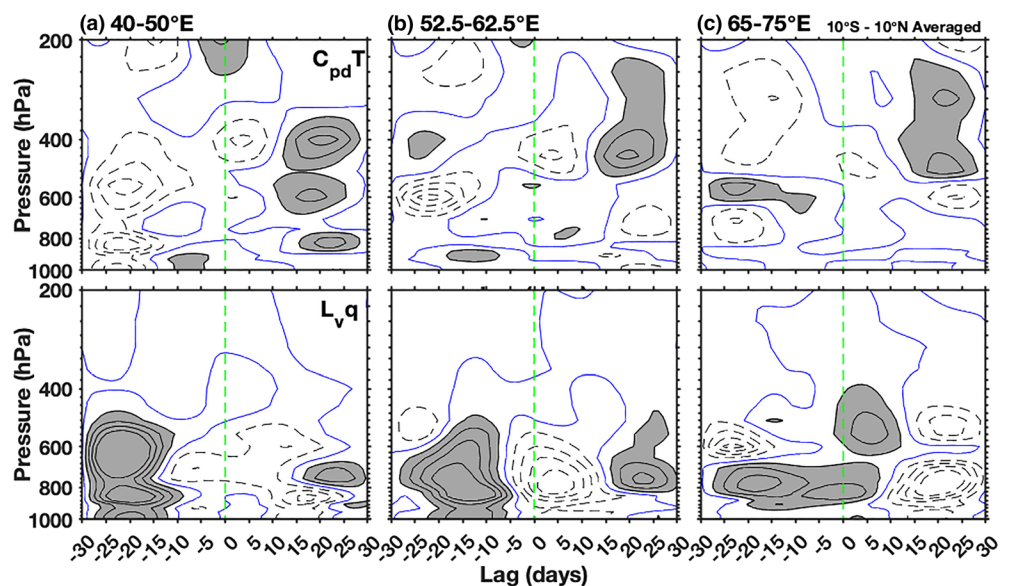
Figure 14. As in Figure 13 but for the (top) $C_{pd}T$ (100 J kg^{-1} interval) and (bottom) $L_v q$ (250 J kg^{-1} interval) terms of the full MSE. The green dashed line denotes the composite MJO initiation day. Positive (negative) values are shaded (non-shaded) gray in solid (dashed) contours. The zero contour is indicated in blue.

Figure 15. Box averaged vertical distribution of MSEA (J kg^{-1}) terms (C_pT, left; L_vq, right) for 2010. Positive (negative) values are shaded (non-shaded) gray in solid (dashed) contours. The red dashed line denotes 20 September. The zero contour is omitted, and the contour interval is 250 J kg^{-1}. The pressure axis is log$_{10}$ scaled to reflect nonlinear atmospheric pressure scaling.

present 15 days prior to the convective peak in the 52.5–62.5°E and 65–75°E boxes primarily below 800 hPa. The low-level positive L_vq would be conducive to shallow convection that then can vertically transport high MSE to the upper levels (Kemball-Cook & Weare, 2001). This shows that significant atmospheric moistening was preceding the convective initiation of the primary MJO event, thus conditioning the atmosphere to deep convective instability. Additionally, midtropospheric cooling is observed as negative C_pT anomalies at this same time in a similar manner to the composite presented.

What is interesting with the 2010 event, however, is the timing of the MSE components. While the moistening is coupled with the necessary cooling of the atmosphere, the timings of the dominant moisture and temperature signals show that MSE is still increasing post-initiation rather than discharging. This would suggest that the 2010 primary MJO was still in the processes of developing its deep convective tower at the time of initiation as opposed to being fully developed already, which is supported by Figure 2. The OLR of Figure 2 was still not yet at its convective peak yet but developed into it quickly after initiation, and that same pattern is observed in the MSE profile. SST is a contributing factor for MSE growth (Arnold et al., 2013), and the predominantly colder SST of the Indian Ocean during the prevailing La Niña conditions (Kug & Kang, 2006) could have contributed to the delayed MSE growth observed. The MSE components of 2015 followed a more similar pattern to the composite of Figure 13. The MJO initiation was preceded by a buildup of moisture coupled with atmospheric cooling that synchronizes well with the rising SST as the same time. The El Niño conditions leading to a generally warmer Indian Ocean would mean that the MSE profile was
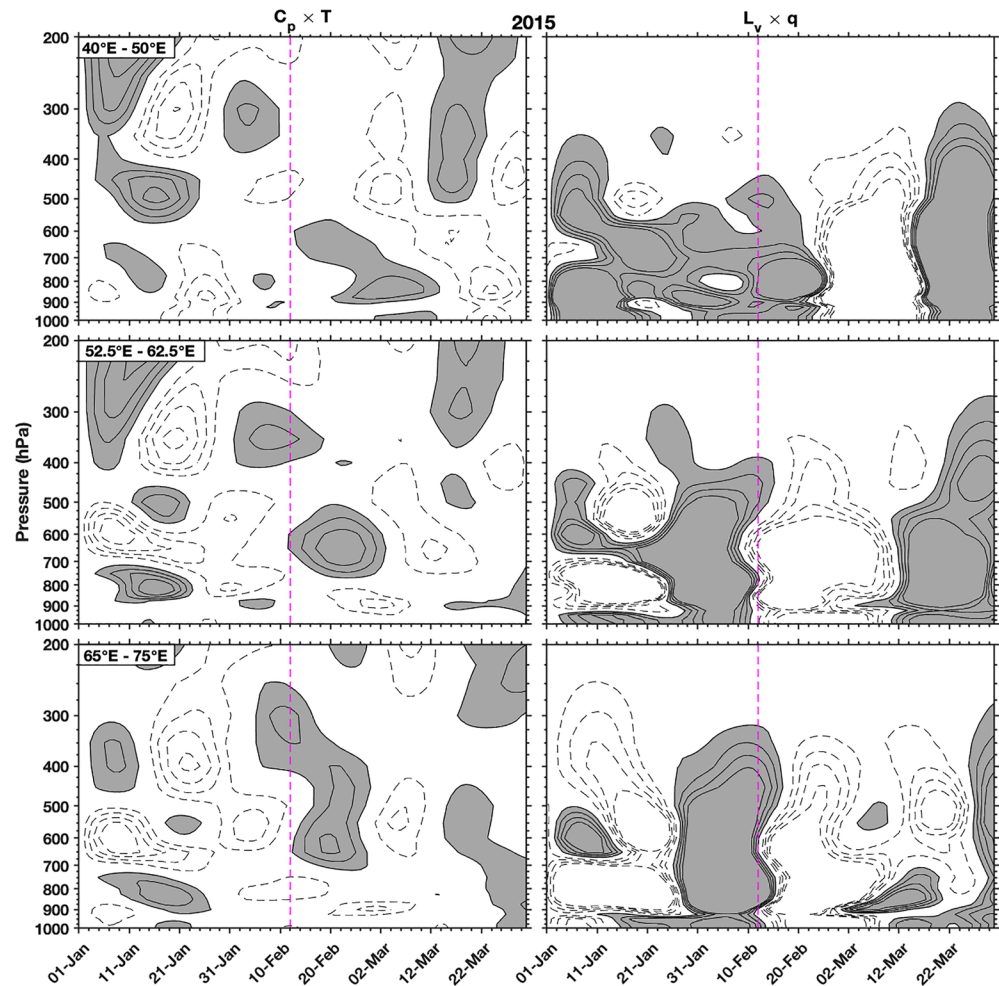
Figure 16. As in Figure 15 but for 2015. The magenta dashed line denotes 12 February.

generated faster than during the La Niña conditions of 2010. The recharge and discharge of MSE surrounding the 2015 MJO are also synchronous with the OLR pattern of Figure 3. The 2015 OLR is much more developed near its peak at the time of initiation and begins to decrease shortly after, which would manifest in the MSE profile as the negative moisture term values due to elevated precipitation from the MJO (Kemball-Cook & Weare, 2001; Sobel et al., 2014).

4. Conclusions

Synchronously examining oceanic and atmospheric parameters is crucial for understanding a more complete picture of MJO initiation over the Indian Ocean region, as preconditioning signals are apparent in both. In this study, we examined two primary MJO event case studies in 2010 and 2015 and the precursor signals in both the atmosphere and ocean in order to understand how the two relate to each other in the initiation process. The two events chosen were selected based on the coexistence of El Niño and La Niña phases such that differences in initiation can be attributed to such variability.

The convective signal of the 2010 event was shown to persist across the Indian Ocean but rapidly decayed over the central and eastern Pacific Ocean due to the predominant La Niña conditions, as the cold waters would have reduced favorability for convective growth. Conversely, the 2015 event persisted strongly across the equatorial Pacific Ocean, even completing a full circumnavigation, due to the warm waters of the strong El Niño, which became one of the strongest, if not the strongest, El Niño ever observed. SST surrounding the initiation of the 2015 event was shown to have a stronger signal than the 2010 event thanks to the El Niño conditions as well. This provided for an overall stronger and quicker response of MSE. The La Niña

conditions of 2010 provided for a slower development of MSE such that the primary MJO would have taken longer to develop to its peak convective strength. What is interesting, however, is that the MFC observed between the two events is greater during the 2010 MJO with a La Niña than the 2015 MJO with an El Niño. Stronger moisture convergence is observed during 2010 than in 2015, which suggests that the La Niña favored stronger convergence over the Indian Ocean despite the colder temperature that would typically be less favorable for convective growth. This warrants further examination as observational abundance increases in the future.

A distinct intraseasonal coupling of the ocean and atmosphere is observed, where ocean warming and boundary layer moisture intrusion moistens and destabilizes the lower atmosphere and preconditions the Indian Ocean region for deep convection. Over 1 billion people in India are affected yearly by the Indian monsoon, which is known to be influenced by the MJO. In addition, the MJO can even affect Atlantic (Klotzbach, 2010) and Pacific Ocean tropical cyclones (Sobel & Maloney, 2000), ocean currents (Mysak & Mertz, 1984) and biology (Resplandy et al., 2009), and even atmospheric aerosols (Langley DeWitt et al., 2013). As such a highly coupled phenomenon, it becomes increasingly important to monitor the MJO by considering both the ocean and atmosphere simultaneously such that prediction efforts can improve based on air-sea preconditioning signals. These results show that preconditioning signals in both the ocean and atmosphere can be observed primarily 1 to 2 weeks before the convective peak, suggesting that if these signals are observed in advance then an MJO event may be predictable. In addition, variability of initiation conditions during varying ENSO phases is observed. As observations become more abundant, however, it becomes increasingly more crucial to make these observations as more primary MJO events are present that coexist with the phases of ENSO. It is important to note, however, that the limited availability of coexisting events with data provides for less robust results. As such, it is crucial for further studies to examine this relationship further as more data and coexisting events become available. Satellite-derived methods have improved over the years such that our observational capabilities have exponentially increased, and it will become even more important to use the latest methods in the future.

Data Availability Statement

The RMMI is provided by the Australian Government's Bureau of Meteorology and is accessible online (at http://www.bom.gov.au/climate/mjo/graphics/rmm.74toRealtime.txt). The OMI is provided courtesy of Kiladis et al. (2014). The ERA5 atmospheric data were obtained from the European Center for Medium-Range Weather Forecasts and are available online at the Copernicus Climate Date Store (CDS; https://cds.climate.copernicus.eu/). Interpolated OLR data are provided by the NOAA/OAR/ESRL PSD and available online (at https://www.esrl.noaa.gov/psd/). The GLORYS12V1 reanalysis data are provided by the Copernicus Marine Environment Monitoring Service (CMEMS) and available online (at http://marine.copernicus.eu/). The altimetry data are managed and provided by CMEMS (available online from http://marine.copernicus.eu/services-portfolio/access-to-products/?option=com_csw%view=details%product_id=SEALEVEL_GLO_PHY_L4_REP_OBSERVATIONS_008_047). SST from the AVHRR is available online at https://www.esrl.noaa.gov/psd/data/gridded/data.noaa.oisst.v2.highres.html and provided by NOAA/OAR/ESRL PSD. CMC GHRSST is distributed by NASA/JPL PODAAC and available online (at https://podaac.jpl.nasa.gov/dataset/CMC0.2deg-CMC-L4-GLOB-v2.0).

References

Arnold, N. P., Kuang, Z., & Tziperman, E. (2013). Enhanced MJO-like variability at high SST. *Journal of Climate*, *26*(3), 988–1001. https://doi.org/10.1175/JCLI-D-12-00272.1

Ashok, K., Guan, Z., Saji, N. H., & Yamagata, T. (2004). Individual and combined influences of ENSO and the Indian Ocean dipole on the Indian summer monsoon. *Journal of Climate*, *17*(16), 3141–3155. https://doi.org/10.1175/1520-0442(2004)017<3141:IACIOE>2.0.CO;2

Ashok, K., Guan, Z., & Yamagata, T. (2001). Impact of the Indian Ocean dipole of the relationship between the Indian monsoon rainfall and ENSO. *Geophysical Research Letters*, *28*(23), 4499–4502. https://doi.org/10.1029/2001GL013294

Banacos, P. C., & Schultz, D. M. (2005). The use of moisture flux convergence in forecasting convective initiation: Historical and operational perspectives. *Weather Forecasting*, *20*(3), 351–366. https://doi.org/10.1175/WAF858.1

Bellenger, H., Yoneyama, K., Katsumata, M., Nishizawa, T., Yasunaga, K., & Shirooka, R. (2015). Observation of moisture tendencies related to shallow convection. *Journal of Atmospheric Science*, *72*(2), 641–659. https://doi.org/10.1175/JAS-D-14-0042.1

Carbone, R. E., & Li, Y. (2015). Tropical oceanic rainfall and sea surface temperature structure: Parsing causation from correlation in the MJO. *Journal of Atmospheric Science*, *72*(7), 2703–2718. https://doi.org/10.1175/JAS-D-14-0226.1

Chao, Y., Li, Z., Farrara, J. D., & Huang, P. (2009). Blended sea surface temperatures from multiple satellites and in-situ observations for coastal oceans. *Journal of Atmospheric and Oceanic Technology*, *26*(7), 1415–1426. https://doi.org/10.1175/2009JTECHO592.1

Chelton, D. B., de Szoeke, R. A., Schalax, M. G., El Naggar, K., & Siwertz, N. (2003). Equatorially trapped Rossby waves in the presence of meridionally sheared baroclinic flow in the Pacific Ocean. *Progress in Oceanography*, *56*(2), 323–380. https://doi.org/10.1016/S0079-6611(03)00008-9

Chelton, D. B., DeSzoeke, R. A., Schlax, M. G., El Naggar, K., & Siwertz, N. (1998). Geographical variability of the first baroclinic Rossby radius of deformation. *Journal of Physical Oceanography*, *28*(3), 433–460. https://doi.org/10.1175/1520-0485(1998)028<0433:GVOTFB>2.0.CO;2

De Deckker, P. (2016). The Indo-Pacific Warm Pool: Critical to world oceanography and world climate. *Geoscience Letters*, *3*, 20. https://doi.org/10.1186/s40562-016-0054-3

Ducet, N., Le Traon, P. Y., & Reverdin, G. (2000). Global high-resolution mapping of ocean circulation from TOPEX/Poseidon and ERS-1 and-2. *Journal of Geophysical Research*, *105*(C8), 19,477–19,498. https://doi.org/10.1029/2000JC900063

Grunseich, G., & Subrahmanyam, B. (2012). Detection of the Madden-Julian oscillation in the Indian Ocean from satellite altimetry. *IEEE Geoscience and Remote Sensing Letters*, *10*(3), 441–445. https://doi.org/10.1109/LGRS.2012.2208261

Grunseich, G., Subrahmanyam, B., & Wang, B. (2013). The Madden-Julian oscillation detected in Aquarius salinity observations. *Geophysical Research Letters*, *40*, 5461–5466. https://doi.org/10.1002/2013GL058173

Hendon, H. H., Wheeler, M. C., & Zhang, C. (2007). Seasonal dependence of the MJO-ENSO relationship. *Journal of Climate*, *20*(3), 531–543. https://doi.org/10.1175/JCLI4003.1

Hersbach, H., Bell, B., Berrisford, P., Horányi, A., Muñoz Sabater, J., Nicolas, J., et al. (2019). Global reanalysis: Goodbye ERA-Interim, hello ERA5. *ECMWF Newsletter*, *159*, 17–24. https://doi.org/10.12957/vf291hehd7

Hong, C., Hsu, H., Tseng, W., Lee, M., Chow, C., & Jiang, L. (2017). Extratropical forcing triggered the 2015 Madden-Julian oscillation-El Niño event. *Scientific Reports*, *7*, 46692. https://doi.org/10.1038/srep46692

Inness, P. M., & Slingo, J. M. (2003). Simulation of the Madden-Julian oscillation in a coupled general circulation model. Part I: Comparison with observations and an atmosphere-only GCM. *Journal of Climate*, *16*(3), 345–364. https://doi.org/10.1175/1520-0442(2003)016<0345:SOTMJO>2.0.CO;2

Inness, P. M., Slingo, J. M., Guilyardi, E., & Cole, J. (2003). Simulation of the Madden-Julian oscillation in a coupled general circulation model. Part II: The role of the basic state. *Journal of Climate*, *16*(3), 365–382. https://doi.org/10.1175/1520-0442(2003)016<0365:SOTMJO>2.0.CO;2

Izumo, T., Masson, S., Vialard, J., de Montegut, C. B., Behera, S. K., Madec, G., et al. (2010). Low- and high-frequency Madden–Julian oscillations in austral summer: Interannual variations. *Climate Dynamics*, *35*(4), 669–683. https://doi.org/10.1007/s00382-009-0655-z

Jensen, T. G., Shinoda, T., Chen, S., & Flatau, M. (2015). Ocean response to CINDY/DYNAMO MJOs in air-sea-coupled COAMPS. *Journal of the Meteorological Society of Japan*, *93A*(0), 157–178. https://doi.org/10.2151/jmsj.2015-049

Kemball-Cook, S. R., & Weare, B. C. (2001). The onset of convection in the Madden-Julian oscillation. *Journal of Climate*, *14*(5), 780–793. https://doi.org/10.1175/1520-0442(2001)014<0780:TOOCIT>2.0.CO;2

Kiladis, G. N., Dias, J., Straub, K. H., Wheeler, M. C., Tulich, K., Kikuchi, K., et al. (2014). A comparison of OLR and circulation based indices for tracking the MJO. *Monthly Weather Review*, *142*(5), 1697–1715. https://doi.org/10.1175/MWR-D-13-00301.1

Klotzbach, P. J. (2010). On the Madden-Julian oscillation-Atlantic hurricane relationship. *Journal of Climate*, *23*(2), 282–293. https://doi.org/10.1175/2009JCLI2978.1

Kug, J., & Kang, I. (2006). Interactive feedback between ENSO and the Indian Ocean. *Journal of Climate*, *19*(9), 1784–1801. https://doi.org/10.1175/JCLI3660.1

Langley DeWitt, H., Coffman, D. J., Schultz, K. J., Alan Brewer, W., Bates, T. S., & Quinn, P. K. (2013). Atmospheric aerosol properties over the equatorial Indian Ocean and the impact of the Madden-Julian Oscillation. *Journal of Geophysical Research: Atmospheres*, *118*, 5736–5749. https://doi.org/10.1002/jgrd.50419

Lau, K., & Shen, S. (1988). On the dynamics of intraseasonal oscillations and ENSO. *Journal of Atmospheric Science*, *45*(12), 1781–1797. https://doi.org/10.1175/1520-0469%281988%29045<1781%3AOTDOIO>2.0.CO%3B2

Le Traon, P. Y., Nadal, F., & Ducet, N. (1998). An improved mapping method of multisatellite altimeter data. *Journal of Atmospheric and Oceanic Technology*, *15*(2), 522–534. https://doi.org/10.1175/1520-0426(1998)015<0522:AIMMOM>2.0.CO;2

Li, T., Zhao, C., Hsu, P., & Nasuno, T. (2015). MJO initiation processes over the tropical Indian Ocean during DYNAMO/CINDY2011. *Journal of Climate*, *28*(6), 2121–2135. https://doi.org/10.1175/JCLI-D-14-00328.1

Liebmann, B., & Smith, C. A. (1996). Description of a complete (interpolated) outgoing longwave radiation dataset. *Bulletin of the American Meteorological Society*, *77*, 1275–1277.

Madden, R. A., & Julian, P. R. (1971). Detection of a 40–50 day oscillation in the zonal wind in the tropical Pacific. *Journal of Atmospheric Sciences*, *28*(5), 702–708. https://doi.org/10.1175/1520-0469(1971)028<0702:DOADOI>2.0.CO;2

Madden, R. A., & Julian, P. R. (1972). Description of global-scale circulation cells in the tropics with a 40–50 day period. *Journal of Atmospheric Sciences*, *29*(6), 1109–1123. https://doi.org/10.1175/1520-0469(1972)029<1109:DOGSCC>2.0.CO;2

Madden, R. A., & Julian, P. R. (1994). Observations of the 40–50-day tropical oscillation—A review. *Monthly Weather Review*, *122*(5), 814–837. https://doi.org/10.1175/1520-0493(1994)122<0814:OOTDTO>2.0.CO;2

Maloney, E. D. (2009). The moist static energy budget of a composite tropical intraseasonal oscillation in a climate model. *Journal of Climate*, *22*(3), 711–729. https://doi.org/10.1175/2008JCLI2542.1

Maloney, E. D., & Hartmann, D. L. (1998). Frictional moisture convergence in a composite life cycle of the Madden-Julian oscillation. *Journal of Climate*, *11*(9), 2387–2403. https://doi.org/10.1175/1520-0442(1998)011<2387:FMCIAC>2.0.CO;2

Marshall, A. G., Alves, O., & Hendon, H. H. (2008). An enhanced moisture convergence-evaporation feedback mechanism for MJO air-sea interaction. *Journal of Atmospheric Science*, *65*(3), 970–986. https://doi.org/10.1175/2007JAS2313.1

Matthews, A. J. (2008). Primary and successive events in the Madden-Julian oscillation. *Quarterly Journal of the Royal Meteorological Society*, *134*(631), 439–453. https://doi.org/10.1002/qj.224

McCreary, J. P. (1983). A model of tropical ocean-atmosphere interaction. *Monthly Weather Review*, *111*(2), 370–387. https://doi.org/10.1175/15200493(1983)111<0370:AMOTOA>2.0.CO;2

Moon, J. Y., Wang, B., & Ha, K. J. (2011). ENSO regulation of MJO teleconnection. *Climate Dynamics*, *37*(5-6), 1133–1149. https://doi.org/10.1007/s00382-010-0902-3

Morita, J., Takayabu, Y. N., Shige, S., & Kodama, Y. (2006). Analysis of rainfall characteristics of the Madden-Julian oscillation using TRMM satellite data. *Dynamics of Atmospheres and Oceans*, *42*(1-4), 107–126. https://doi.org/10.1016/j.dynatmoce.2006.02.002

Mysak, L. A., & Mertz, G. J. (1984). A 40- to 60-day oscillation in the source region of the Somali Current during 1976. *Journal of Geophysical Research*, *89*(C1), 711–715. https://doi.org/10.1029/JC089iC01p00711

Neelin, J. D., & Held, I. M. (1987). Modeling tropical convergence based on the moist static energy budget. *Monthly Weather Review*, *115*(1), 3–12. https://doi.org/10.1175/1520-0493(1987)115<0003:MTCBOT>2.0.CO;2

Oliver, E. C. J., & Thompson, K. R. (2010). Madden-Julian oscillation and sea level: Local and remote forcing. *Journal of Geophysical Research*, *115*, C01003. https://doi.org/10.1029/2009jc005337

Picaut, J., Ioualalen, M., Menkes, C., Delcroix, T., & McPhaden, M. J. (1994). Mechanisms of the zonal displacements of the Pacific warm pool: Implications for ENSO. *Science*, *274*, 1486–1489.

Resplandy, L., Vialard, J., Lévy, M., Aumont, O., & Dandonneau, Y. (2009). Seasonal and intraseasonal biogeochemical variability in the thermocline ridge of the southern tropical Indian Ocean. *Journal of Geophysical Research*, *114*, C07024. https://doi.org/10.1029/2008JC005246

Reynolds, R. W., Smith, T. M., Liu, C., Chelton, D. B., Casey, K. S., & Schlax, M. G. (2007). Daily high-resolution blended analyses for sea surface temperature. *Journal of Climate*, *20*(22), 5473–5496. https://doi.org/10.1175/2007JCLI1824.1

Roman-Stork, H. L., Subrahmanyam, B., & Murty, V. S. N. (2019). Quasi-biweekly oscillations in the Bay of Bengal is observations and model simulations. *Deep Sea Research Part II*, *168*, 104609. https://doi.org/10.1016/j.dsr2.2019.06.017

Rydbeck, A. V., & Jensen, T. G. (2017). Ocean impetus for convective onset of the Madden-Julian oscillation in the western Indian Ocean. *Journal of Climate*, *30*(11), 4299–4316. https://doi.org/10.1175/JCLI-D-16-0595.1

Saji, N. H., Goswami, B. N., Vinayachandran, P. N., & Yamagata, T. (1999). A dipole mode in the tropical Indian Ocean. *Nature*, *401*(6751), 360–363. https://doi.org/10.1038/43854

Santoso, A., Mcphaden, M. J., & Cai, W. (2017). The defining characteristics of ENSO extremes and the strong 2015/2016 El Niño. *Reviews of Geophysics*, *55*, 1079–1129. https://doi.org/10.1002/2017RG000560

Shinoda, T., Jensen, T. G., Flatau, M., Chen, S., Han, W., & Wang, C. (2013). Large-scale oceanic variability associated with the Madden-Julian oscillation during the CINDY/DYNAMO field campaign from satellite observations. *Remote Sensing*, *5*(5), 2072–2092. https://doi.org/10.3390/rs5052072

Shoup, C. G., Subrahmanyam, B., & Roman-Stork, H. L. (2019). Madden-Julian oscillation-induced sea surface salinity variability as detected in satellite-derived salinity. *Geophysical Research Letters*, *46*, 9748–9756. https://doi.org/10.1029/2019GL083694

Sobel, A., Wang, S., & Kim, D. (2014). Moist static energy budget of the MJO during DYNAMO. *Journal of Atmospheric Science*, *71*(11), 4276–4291. https://doi.org/10.1175/JAS-D-14-0052.1

Sobel, A. H., & Maloney, E. D. (2000). Effect of ENSO and the MJO on western North Pacific tropical cyclones. *Geophysical Research Letters*, *27*(12), 1739–1742. https://doi.org/10.1029/1999GL011043

Straub, K. H. (2013). MJO initiation in the real-time multivariate MJO index. *Journal of Climate*, *26*(4), 1130–1151. https://doi.org/10.1175/JCLI-D-12-00074

Tang, Y., & Yu, B. (2008). MJO and its relationship to ENSO. *Journal of Geophysical Research*, *113*, D14106. https://doi.org/10.1029/2007JD009230

Trott, C. B., & Subrahmanyam, B. (2019). Detection of intraseasonal oscillations in the Bay of Bengal using altimetry. *Atmospheric Science Letters*, *20*, e920. https://doi.org/10.1002/asl.920

Wang, B. (1988). Dynamics of tropical low-frequency waves: An analysis of the moist Kelvin wave. *Journal of Atmospheric Science*, *45*(14), 2051–2065. https://doi.org/10.1175/1520-0469(1988)045<2051:DOTLFW>2.0.CO;2

Wang, L., Kodera, K., & Chen, W. (2012). Observed triggering of tropical convection by a cold surge: Implications for MJO initiation. *Quarterly Journal of the Royal Meteorological Society*, *138*(668), 1740–1750. https://doi.org/10.1002/qj.1905

Webber, B. G., Matthews, A. J., & Heywood, K. J. (2010). A dynamical ocean feedback mechanism for the Madden-Julian Oscillation. *Quarterly Journal of the Royal Meteorological Society*, *136*, 740–754. https://doi.org/10.1002/qj.604

Webber, B. G., Matthews, A. J., Heywood, K. J., & Stevens, D. P. (2012). Ocean Rossby waves as a triggering mechanism for primary Madden–Julian events. *Quarterly Journal of the Royal Meteorological Society*, *138*(663), 514–527. https://doi.org/10.1002/qj.936

Webster, P. J., Moore, A., Loschnigg, J., & Leban, M. (1999). Coupled ocean-atmosphere dynamics in the Indian Ocean during 1997–1998. *Nature*, *401*(6751), 356–360. https://doi.org/10.1038/43848

Wheeler, M. C., & Hendon, H. H. (2004). An all-season real-time multivariate MJO index: Development of an index for monitoring and prediction. *Monthly Weather Review*, *132*(8), 1917–1932. https://doi.org/10.1175/1520-0493(2004)132<1917:AARMMI>2.0.CO;2

Wilson, E. A., Gordon, A. L., & Kim, D. (2013). Observations of the Madden Julian oscillation during Indian Ocean dipole events. *Journal of Geophysical Research: Atmospheres*, *118*, 2588–2599. https://doi.org/10.1002/jgrd.50241

Woolnough, S. J., Vitart, F., & Balmaseda, M. A. (2007). The role of the ocean in the Madden-Julian oscillation: Implications for MJO prediction. *Quarterly Journal of the Royal Meteorological Society*, *133*(622), 117–128. https://doi.org/10.1002/qj.4

Zhang, C. (2005). Madden-Julian oscillation. *Reviews of Geophysics*, *43*, RG2003. https://doi.org/10.1029/2004RG000158

Zhao, C., Li, T., & Zhou, T. (2013). Precursor signals and processes associated with MJO initiation over the tropical Indian Ocean. *Journal of Climate*, *26*(1), 291–307. https://doi.org/10.1175/JCLI-D-12-00113.1